Sánchez-Arriaga, G.; Naghdi, S. Ionospheric experiment with a low work function tether loop, In: *Journal of guidance, control, and dynamics, 43(2) Feb. 2020, Pp. 212-221.*

DOI: https://doi.org/10.2514/1.G004746

An Ionospheric Experiment with a Low Work Function Tether Loop

G. Sanchez-Arriaga[1] and S. Naghdi[2]
Carlos III University of Madrid, Leganés, 28911,Spain

An entirely passive and free of consumable ionospheric experiment, based on a low work function tether (LWT) loop with a control unit equipped with some basics sensors at its center, is presented. The loop has a torus shape and a hollow cross-section. It is made of an aluminum substrate coated with a low work function material to stimulate electron emission through thermionic and photoelectric effects. The work presents an electrodynamic model for the experiment and studies the current and voltage profiles developed in the anodic and cathodic segments of the LWT due to the motional electric field. Two modes of operation, with and without switches in the loop to interrupt the electric current, are considered. It is shown that the loop is deorbited by the Lorentz force exerted by the ambient magnetic field on the electric current. An analysis of the attitude dynamics in the presence of the gravity gradient and the Lorentz torques reveals that, for a circular equatorial orbit, the position of the loop with its symmetry axis normal to the orbital plane can be spin-stabilized easily. The required instruments and the scientific information that would be provided by the experiment are discussed.

---

[1] Ramón y Cajal Research Fellow, Bioengineering and Aerospace Engineering Department, Avda. de la Universidad 30, 28911, Leganés, Madrid, Spain
[2] Postdoctoral Researcher, Bioengineering and Aerospace Engineering Department, Avda. de la Universidad 30, 28911, Leganés, Madrid, Spain

Nomenclature

A_t = tether cross-sectional area, m^2

B = Earth's magnetic field, T

E = motional electric field, V/m

e = elementary charge, C

h_t = tether thickness, m

I = tether current, A

$\bar{I}_O$ = tensor of inertia about O, kgm^2

J = tether current density, A/m^2

k_B = Boltzmann constant, J/K

m_c = mass of the control unit, kg

m_l = mass of the tether loop, kg

N_0 = plasma density, $1/m^3$

p = generalized momentum

p_t = tether perimeter, m

$\tilde{Q}$ = normalized generalized force

r = loop position vector, m

R_l = loop radius, m

R_t = tether radius, m

r_{sh} = sheath radius, m

s = tether arc length, m

T = temperature, K

V = local bias, V

v = loop velocity, m/s

W_t = tether work function, eV

λ_{De} = electron Debye length, m

μ = Earth's gravitational parameter, m^3/s^2

ρ_t = tether density, kg/m^3

σ_t = tether conductivity, $1/\Omega m$

θ, ψ, ϕ = Tait-Bryan angles, rad

φ = azimuth angle, rad

Subscripts

th = thermionic

ph = photoelectric

e = electron

i = ion

t tether

$\parallel$ = vector component in the plane of the loop

$\perp$ = vector component normal to the plane of the loop

I. Introduction

Ring-like and doughnut-shaped space structures have been proposed for several applications in the past and have inspired the imagination of aerospace engineers and science fiction authors. Some examples are the space settlement studied by NASA in 1975 [10], the space exploration vehicle Nautilus-X [7], and the electric sail [9], which consists of a rotating central hub with tens of electrically charged bare aluminum wires that electrostatically repel fast protons from the solar wind. An electrodynamic structure with a circular shape and electron collectors and emitters disposed on the periphery has been proposed to produce thrust and power [13]. Several complex structures based on tethers have also been considered for a wide range of applications such as an array of tethers for the excitation of a whistler wave-front [20], and also other multi-tether structures to be applied as a large antenna or to provide a physical separation among several connected platforms [15]. The dynamics of tethered satellite systems received significant attention [1, 11, 28]. A particular case is a ring made of satellites linked by tethers [2, 8], a problem that has its foundation on the analysis of a ring rotating around an attracting center, and considered a long time ago by Laplace and Maxwell.

The case of an electrodynamic tether loop raised some controversies in the past. In the standard straight bare tether concept, electrons are collected passively from the ambient plasma by an anodic segment and the circuit is closed by an active electron emitter at a tether tip [24]. Its performance naturally depends on ambient plasma density and magnetic field. In order to circumvent the dependence with plasma density, a closed wire (loop) partially shielded by a superconductor from the

outer magnetic field was proposed [3]. However, since the magnetic field presents negligible spatial variations in the region of interest and no current exchange occurs with the ambient plasma, it was later shown that no net force appears on the loop [25].

A recent concept, named low work function tether (LWT), is here used to propose an experiment based on a ring-shaped (loop) electrodynamic tether. A LWT is a conductor coated with a low work function material that operates passively and with no need for consumable and power: a tether segment captures electrons from the ambient plasma as a standard bare tether, and the complementary segment closes the electric circuit by emitting electrons through thermionic [27] and photoelectric [19] effects. As compared with a straight tether, the ring configuration yields to poor deorbit performance, which is the standard and more natural application of LWTs (see for instance deorbit performance in Geostationary Transfer Orbit in Ref. [21]). However, a loop offers several advantages for a scientific experiment because it would be possible to measure, in real time and throughout the tether, the current and voltage profiles induced by the motional electric field. Moreover, unlike previous tether loop configurations, a net force appears because a current exchange happens with the ambient plasma. Such a force, which is a natural consequence of the relative motion of two conductors (LWT and plasma) with a good electrical contact in the presence of a magnetic field, produces the deorbiting of the loop. Since the LWT is fully passive and involves no consumable, a light and simple experiment could be conducted to obtain valuable scientific information on tether dynamics, the physics of ionospheric plasmas, and its interaction with low work function materials.

The work is organized as follows. Section II discusses the general configuration and geometry of the experiment. The electrodynamic model for the LWT loop is presented in Sec. III, where the equations governing the current and voltage profiles along a curved electrodynamic tether are found. As a byproduct of the analysis, previous models on that topic [14, 18] are briefly revisited. Section IV studies the dynamics of the center of mass of the loop and its attitude. The conclusions of the work are summarized in Sec. V.

II. Description of the experiment

Panels (a)-(c) in Fig. 1 display a sketch of the experimental setup. We consider a LWT loop of radius R_l made of aluminum and coated with a material of work function W_t. The loop defines the $x-y$ plane of a frame of reference named S_L that moves with the tether, and its origin O is at the center of the loop. A basis with unit vectors $\boldsymbol{u_x}$ and $\boldsymbol{u_y}$ spanning the plane of the loop and $\boldsymbol{u_z}$ normal to it is introduced. As shown in panel (b), which is a section by a plane that contains $\boldsymbol{u_z}$ and pass through point O, the tether has an annular cross-section of external radius R_t and thickness h_t. Such a shape provides good mechanical stability while keeping a low mass, two features that cannot be achieved by a simple tape or a solid round tether in a loop configuration. Typical dimensions for R_l, R_t, and h_t in the experiment are tens of meters, few centimeters, and tens of microns, respectively. Therefore, the shape of the LWT loop is a torus with three disparate dimensions, $R_l >> R_t >> h_t$. Moreover, the radius of the loop is also much larger than the electron Debye length, $R_l >> \lambda_{De}$, which is typically a fraction of centimeter in Low Earth Orbit (LEO).

At point O there is a control unit of mass m_c that is electrically connected to some tether points by radial wires. The unit is equipped with same basic sensors, telemetry, and telecommand. For simplicity, we will assume that all the elements of the experiment move as a rigid body and the mass of the radial wires will be neglected. The center of mass of the system coincides with point O and the total mass of the experiment is $m = m_c + m_l \equiv m_c + 2\pi\rho_t A_t R_l$, where ρ_t and $A_t \approx 2\pi R_t h_t$ are the tether density and cross-sectional area. Since the typical size of the control unit is small as compared to R_l, the S_L-components of the tensor of inertia about point O reads

$$\bar{\boldsymbol{I}}_{\boldsymbol{0}} = \frac{m_l R_l^2}{2} \begin{pmatrix} 1 & 0 & 0 \\ 0 & 1 & 0 \\ 0 & 0 & 2 \end{pmatrix} \tag{1}$$

The axes of frame S_L are principal axes of inertia of the loop about point O.

Let us call $s \equiv R_l\varphi$, φ, and $\boldsymbol{I}(s) = I(s)\boldsymbol{u_\varphi}$ to the arc-length, azimuth angle, and electric current of a generic tether cross-section [see panel (c) in Fig. 1]. The tether potential $V_t(s)$ is governed by

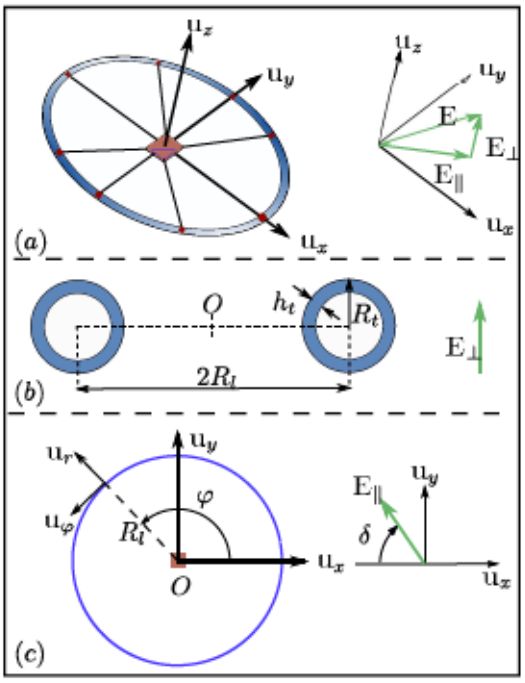

Figure 1 LWT loop configuration. The loop frame (S_L) is the one with the origin at the center of the loop and has unit vectors u_x, u_y and u_z.

Ohm's law $dV_t/ds = -I(\varphi)/\sigma_t A_t$, with σ_t the tether conductivity. On the other hand, the electric field in the highly conductive plasma faraway from the tether, which is at equilibrium, vanishes in a frame linked to the plasma. Therefore, for an observer moving with the loop, a motional electric field $\boldsymbol{E} \approx \boldsymbol{v} \times \boldsymbol{B}$ appears in the faraway plasma due to the tether-to-plasma relative velocity $\boldsymbol{v}$ and the ambient magnetic field B. The plasma potential $V_p(s)$ at a faraway point P, i.e. at a distance large enough from the loop to recover plasma quasi-neutrality, varies due to the motional electric field according to $\boldsymbol{E} = -\nabla V_p$. Writing the distance between O and P as $R = R_l + kr_{sh}$, where k is a factor of order unity and r_{sh} is the sheath radius, and dotting $\boldsymbol{E} = -\nabla V_p$ with the azimuthal unit vector $\boldsymbol{u}_\varphi$ yield

$$\nabla V_p \cdot \boldsymbol{u}_\varphi = \frac{R_l}{R}\frac{dV_p}{ds} = \frac{1}{1 + kr_{sh}/R_l}\frac{dV_p}{ds} \approx \frac{dV_p}{ds} \tag{2}$$

where we assumed that the radius of the loop is much larger than the typical distance that is necessary to recover plasma quasi-neutrality, i.e. $R_l >> kr_{sh}$. Such inequality holds for the typical values of V considered in this work (also note that $R_l >> \lambda_{De}$). After decomposing the motional electric field as $\boldsymbol{E} = \boldsymbol{E}_\parallel + \boldsymbol{E}_\perp = -E_\parallel(\cos\delta \boldsymbol{u}_x - \sin\delta \boldsymbol{u}_y) + E_\perp \boldsymbol{u}_z$, $\boldsymbol{E} = -\nabla V_p$ then gives us

$dV_p/ds = -E_\parallel \sin(\delta + \varphi)$ and the local bias $V(s) \equiv V_t(s) - V_p(s)$ is governed by

$$\frac{dV}{ds} = -\frac{I(s)}{\sigma_t A_t} + E_\parallel \sin\left(\delta + \frac{s}{R_l}\right) \tag{3}$$

Two important features of Eq. (3) linked to previous works about curved electrodynamic tethers may be highlighted. First, unlike the approximate analysis of Ref. [18] that inserted a constant motional electric field reduced by a certain factor related to tether curvature, our system of ordinary differential equations is non-autonomous (the independent variable s appears explicitly). Second, $\boldsymbol{E}$ is not the motional electric field evaluated at the tether (as claimed in [14]), but the electric field at the faraway plasma in a frame linked to the tether. If the radius of curvature is large enough, one has $R_l/R \approx 1$ and the variations of the plasma potential along the tether arc length $s = R_l\varphi$ and $R\varphi$ practically coincide.

Equation (3) is coupled with the electric current $I(s)$, which is given by

$$\frac{dI}{ds} = -p_t \times J(V) \tag{4}$$

where $p_t = 2\pi R_t$ is the external perimeter of the cross-section and $J(V)$ the current density, which depends on the quality of the electric contact between the tether and the plasma. For potential bias yielding electron collection (electron emission) one has $J(V) > 0$ ($J(V) < 0$). The disparate scales in the configuration of the experiment simplify the calculation of J notably. As a first approximation, electron collection and emission is a two-dimensional problem that occurs in the plane displayed in panel (b) of Fig. 1. As previously mentioned, one has $R_l >> \lambda_{sh}$ and interference effects [5, 23] between the two annular sections in the plane can also be ignored in the analysis. Therefore, $J(V)$ can be found by using plasma theory for emissive and infinitely long probes. As shown in Sec. III, J depends on tether properties, such as radius R_t, work function W_t, and photoelectric yield, and also on ambient parameters like the unperturbed plasma density (N_0), and the ratios of electron and ion masses and temperatures (m_e/m_i and T_e/T_i). The integration of Eqs. (3)-(4) with the appropriate boundary conditions gives the current and voltage profiles as a function of ambient parameters and tether properties.

From $I(s)$, interesting quantities such as the Lorentz force and torque about O are found. As a consequence, measuring the current and voltage profiles at each instant during the experiment, as well as the deorbiting decay rate and loop attitude, would provide abundant scientific information about LWT dynamics and its interaction with the ionospheric plasma. From this perspective, the loop configuration is advantageous as compared with a straight tether. First, the current and tether temperature profiles versus φ could be measured by a set of ammeters and thermocouples distributed along the loop. These sensors are represented schematically as red points in panel (a) of Fig. 1]. Second, several tether points could be electrically connected by radial wires to voltmeters on-board the control unit located at the center of the loop, thus providing the potential bias between the control unit and the corresponding tether points. The impedances of the voltmeters are obviously high, and the electrical currents through the radial wires can be ignored. Additionally, if the control unit is equipped with a Langmuir probe, a GPS transponder, and magnetometers, then plasma properties, loop position and velocity vectors, and ambient magnetic field could also be measured in real time. The information of these sensors could be used to estimate the motional electric field and the attitude of the loop. This data, together with the current, voltage, and temperature profiles, could be sent to a ground station for its later analysis.

The proposed experiment could be operated under two different modes if switches are placed at several locations in the tether loop to interrupt the electric current. In the *loop-mode*, the switches are closed, and the current can circulate freely along the full loop. The boundary conditions for Eqs (3)-(4) are periodic: $I(0) = I(L_t)$ and $V(0) = V(L_t)$, with $L_t = 2\pi R_t$ the tether length. In the *arc-mode*, one or more switches are opened for blocking the circulation of the electric current at certain points. The analysis of Eqs. (3)-(4) would then be split into several arcs (its number depending on the configuration of the switches). In this work, we will consider two switches at locations $\varphi_1 = 0$ and $\varphi_2 = \pi$, and their current and voltage profiles within the ranges $0 \leq \varphi \leq \pi$ and $\pi \leq \varphi \leq 2\pi$ are governed by Eqs (3)-(4) with the boundary conditions $I(0) = I(\pi) = 0$ and $I(\pi) = I(2\pi) = 0$, respectively.

III. Electrodynamic model of the LWT loop

A. General considerations

Some simple but still clarifying points can be obtained by making some manipulations of Eqs. (3)-(4) for the *loop-mode*. Setting the left-hand-side (lhs) of (3) multiplied by the right-hand-side (rhs) of (4) equal to the rhs of (3) multiplied by the lhs of (4) and integrating the resulting equation from $\mathbf{0}$ to $\mathbf{2\pi}$ yield

$$\int_0^{2\pi} I(\varphi)\cos\varphi d\varphi = 0 \tag{5}$$

Next, Eq. (3) is multiplied by $\boldsymbol{I}$, Eq. (4) by $\boldsymbol{V}$, and the results are added. The resulting equation is integrated from $\mathbf{0}$ to $\mathbf{2\pi}$ to find

$$\int_0^{2\pi} E_\parallel I\sin\varphi d\varphi = \int_0^{2\pi} \frac{I^2}{\sigma_t A_t} + \int_0^{2\pi} p_t V J d\varphi \tag{6}$$

As shown in Sec. III C the term on the left is a *force integral* that naturally appears when computing the Lorentz power, i.e. the dot product of the Lorentz force by the spacecraft velocity (see Eq. (16)). Such a magnitude is important because it controls the decay rate of the loop according to Eq. (23). Equation (6) then reveals that the Lorentz power supports the ohmic dissipation and the power required to exchange current with the ionospheric plasma.

Another interesting feature of Eqs. (3)-(4) is its non-autonomous character due to the factor $\mathbf{\sin(\delta+\varphi)}$ in Eq. (3). As a consequence, the current-voltage profiles of the loop do not admit the well-known first integral of standard (straight) bare-tether, thus making the system more complex. We finally mention that the motional electric field, involving orbital velocity and Earth magnetic field, is the same for straight and loop-like tethers. However, the tether bias comprises an additional length factor that is in the order of kilometers and tens of meters for straight and loop-like tethers. For that reason, the standard *high-bias* assumption used in the past analyses, which assumes that tether bias energizes attracted electrons well above the thermal energy, may be revisited. Moreover, the external radius of the hollow loop is typically much higher than the one of a solid round tether. As a consequence, a detailed discussion of the current exchange model, i.e. function $\boldsymbol{J(V)}$, is needed.

B. Current exchange model

Function $J(V)$, i.e. the model for the electron capture and emission, is necessary for the integration of Eqs. (3)-(4). It encloses information about the interaction between the LWT and the ambient plasma and, in general, a tough kinetic problem in plasma physics (Langmuir and emissive probe theory) should be solved. Past works on straight tethers used some useful analytical formulae for J like the orbital-motion-limited (OML) law [12] for the electron capture along an anodic segment with sufficiently small radius [22], and the Richardson-Dushman law [17] for a cathodic segment with negligible photoelectric and space charge effects. However, the parametric conditions for the loop in terms of bias and radius, and also the existence of a space charge limited segment, requires a more general model.

This work borrows the model for $J(V)$ from a recent study that presented the Orbital Motion Theory (OMT) for infinitely long Langmuir and emissive probes with cylindrical cross-sections [4]. Such a model is valid for collision-less and stationary plasmas with no trapped electrons. Given the following dimensionless parameters

$$\frac{m_i}{m_e}, \frac{T_i}{T_e}, \frac{R_t}{\lambda_{De}}, \frac{T_{th}}{T_e}, \frac{T_{ph}}{T_e}, \frac{N_{th}}{N_0}, \frac{N_{ph}}{N_0}, \frac{eV}{k_B T_e}, \tag{7}$$

it provides the normalized current density $j \equiv J/J_0$ by solving the Vlasov-Poisson system numerically. Here

$$J_0 = eN_0\sqrt{\frac{k_B T_e}{2\pi m_e}} \tag{8}$$

is the electron thermal current and, in Eq. (7), T_{th} and T_{ph} are the temperatures of the electrons emitted through thermionic and photoelectric effects at the probe, respectively. Similarly, N_{th} and N_{ph} are the emitted electron densities, that are directly linked to tether work function W_t, temperature T_t, photoelectric yield, and optical properties if a half-Maxwellian distribution function is assumed for the emitted electrons (find detailed models in Ref. [19]). We highlight that the j-curves provided by the theory fully account for space charge effects and are valid for any R/λ_{De} ratio.

Tables 1 and 2 show the parameters used in this work for both the electrical model in Sec. III and the dynamic analysis of Sec. IV. They correspond to typical ambient and design values for a mission in LEO at an altitude around $800km$. Fig. 2 shows the j versus eV/k_BT_e curve computed for those values using the kinetic model of Ref. [4]. For this particular set of parameters, the floating potential, i.e. the potential value giving $j = 0$, is $eV_f/k_BT_e \approx 1.94$. The emitted current for very low bias is $j(eV/kT_e \to -\infty) \approx -6$. For high bias, although the chosen radius exceeds the maximum radius for OML current [22], one almost recovers the OML current $J \approx J_{OML} = 2\sqrt{eV/\pi k_BT_e}$.

Variable	Value	Variable	Value
N_0	$10^{11}m^{-3}$	R_l	$20m$
T_e	$0.15eV$	R_t	$1.5cm$
T_i	$0.15eV$	h_t	$30\mu m$
ρ_t	$2700kg/m^3$	σ_t	$3.54 \times 10^7 1/\Omega m$
W_t	$1.4eV$	T_t	$500K$
T_{ph}	$0.25eV$	T_{th}	$500K$
r_0	$7171km$	J_0	$0.001A/m^2$
m_l	$1kg$	m_c	$4kg$

Table 1 Ambient and tether parameters used in the analysis

Variable	Value	Variable	Value
T_i/T_e	1	R_t/λ_{De}	1.65
T_{th}/T_e	0.29	T_{ph}/T_e	1.67
N_{th}/N_0	2.1	N_{ph}/N_0	1.4
m_i/m_e	29378		

Table 2 Dimensionless parameters found from Table 1

C. Current and voltage profiles

After introducing the dimensionless current $\tilde{I} \equiv I/p_tR_lJ_0$ and bias $\tilde{V} = eV/k_BT_e$, Eqs. (3)-(4) become

$$\frac{d\tilde{V}}{d\varphi} = -\alpha\tilde{I} + \tilde{E}_{\parallel}\sin(\delta + \varphi) \tag{9}$$

$$\frac{d\tilde{I}}{d\varphi} = -j(\tilde{V}) \tag{10}$$

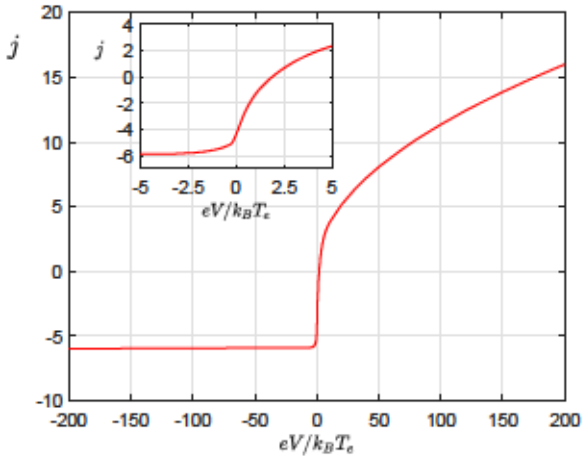

Figure 2 Normalized current density j versus eV/k_BT_e.

where $\alpha \equiv eJ_0p_tR_t^2/\sigma_tA_tk_BT_e$ and $\tilde{E}_\parallel \equiv eR_tE_\parallel/k_BT_e$. The normalized average current for a generic arc denoted by superscript i and covering the range $\varphi_0^i \leq \varphi \leq \varphi_f^i$ is

$$\tilde{I}_{av}^i \equiv \int_{\varphi_0^i}^{\varphi_f^i} \tilde{I} d\varphi_i = \\ = \frac{\tilde{E}_\parallel \left[\cos(\delta+\varphi_0^i) - \cos\left(\delta+\varphi_f^i\right)\right] + \tilde{V}(\varphi_0^i) - \tilde{V}\left(\varphi_f^i\right)}{\alpha} \tag{11}$$

where we used Eq. (9). The *loop-mode*, which has $\varphi_0^i = 0$ and $\varphi_f^i = 2\pi$ and the boundary condition $\tilde{V}(0) = \tilde{V}(2\pi)$, has zero average current.

For the experiment considered in this work (see Tables 1 and 2), the tether is short enough to make ohmic effects negligible because one finds $\alpha = 0.0026$. For that reason, we here ignore the first term in the right-hand side of Eq. (9) and integrate the equations to find the profiles

$$\tilde{V}(\varphi) = \tilde{V}_0 + \tilde{E}_\parallel \left[\cos\left(\delta+\varphi_0^i\right) - \cos\left(\delta+\varphi\right)\right] \tag{12}$$

$$\tilde{I}(\varphi) = \tilde{I}_0 + \tilde{I}_1(\varphi) \tag{13}$$

where $\tilde{V}_0$ and $\tilde{I}_0$ are two constants that should be found with the appropriate boundary conditions and we defined the function

$$\tilde{I}_1(\varphi) \equiv -\int_{\varphi_0^i}^{\varphi} j\left[\tilde{V}(\varphi')\right] d\varphi' \tag{14}$$

For a tether arc, the boundary condition $\tilde{I}(\varphi_0^i) = 0$ gives $\tilde{I}_0 = 0$, and $\tilde{I}(\varphi_f^i) = 0$ becomes $\tilde{I}_1(\varphi_f) = 0$, which can be solved to find $\tilde{V}_0$. Regarding the *loop-mode*, the condition $V(0) = V(2\pi)$ is always satisfied and $\tilde{I}(0) = \tilde{I}(2\pi)$ requires $\tilde{I}_1(2\pi) = 0$, that again gives the value of $\tilde{V}_0$. In principle, constant $\tilde{I}_0$ would be free for this ideal model (without ohmic effect). However, for finite ohmic effects, we know from Eq. (11) that the average current in a loop vanishes and the physical solution without ohmic effects satisfies

$$\tilde{I}_0 = -\frac{1}{2\pi}\int_0^{2\pi} \tilde{I}_1(\varphi)d\varphi \tag{15}$$

Panels (a) and (b) in Fig. 3 show sketches of the normalized current and voltage profiles in the *loop-mode* without ohmic effects, $\tilde{E}_{\parallel} = 30$ and $\delta = 0$ and the $j(\tilde{V})$ curve of Fig. 2. The solid (black) line represents the loop and the dash-dotted (red) and dashed (blue) lines are the current and voltage profiles, where their radial distances to the origin are larger and smaller than the radius of the loop if they are positive or negative, respectively. Electron collection and emission happen around the ranges $\pi/2 \lesssim \varphi \lesssim 3\pi/2$ and $-\pi/2 \lesssim \varphi \lesssim \pi/2$, respectively. The current is positive (along $\boldsymbol{u}_\varphi$) and negative (opposite to $\boldsymbol{u}_\varphi$) for $0 \lesssim \varphi \lesssim \pi$ and $\pi \lesssim \varphi \lesssim 2\pi$.

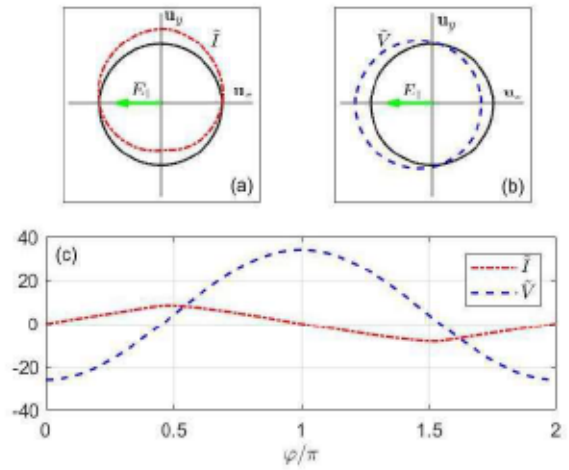

Figure 3 Panels (a) and (b) display sketches of the normalized current and voltage profiles for a loop with $\tilde{E}_{\parallel} = 30$, $\delta = 0$, and no ohmic effects. Panel (c) shows the profiles versus φ.

Figure 4 shows the current and voltage profiles for a loop with switches interrupting the current at points $\varphi = 0$ and $\varphi = \pi$, $\tilde{E}_{\parallel} = 30$, $\delta = \pi/4$, and no ohmic effects. Therefore, it corresponds to

two independent tether arcs with vanishing current and discontinuous bias at their ends.

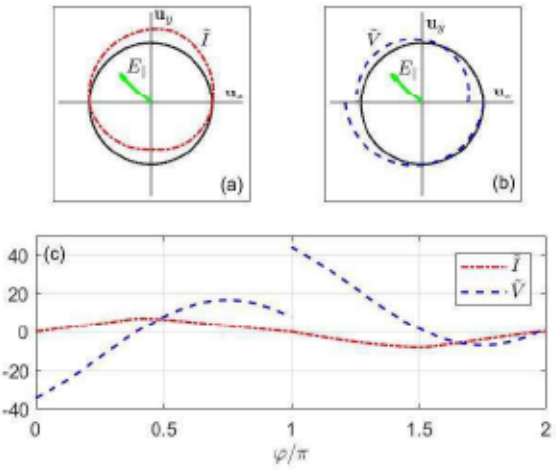

Figure 4 Panel (a) and (b) display sketches of the normalized current and voltage profiles for two arcs of length πR_l, with $\tilde{E}_\parallel = 30$, $\delta = \pi/4$, and no ohmic effects. Panel (c) shows the profiles versus φ.

D. Lorentz drag and torque

Once the voltage and current profiles are known, important quantities for the analysis of the dynamics of the loop can be found. One of them is the component of the Lorentz force $\boldsymbol{F}_L^i$ along the opposite direction to the loop velocity

$$F_D^i \equiv -\boldsymbol{F}_L^i \cdot \frac{\boldsymbol{v}}{v} = -\frac{R_l \boldsymbol{v}}{v} \cdot \int_{\varphi_0^i}^{\varphi_f^i} I(s)\boldsymbol{u}_\varphi \times \boldsymbol{B} d\varphi = \frac{R_l}{v}\int_{\varphi_0^i}^{\varphi_f^i} I(\varphi)\boldsymbol{u}_\varphi \cdot \boldsymbol{E}_\parallel d\varphi \equiv \frac{p_t R_l^2 J_0 E_\parallel}{v}\tilde{f}_D^i \tag{16}$$

where we used that $\boldsymbol{v}\cdot(\boldsymbol{u}_\varphi \times \boldsymbol{B}) = -\boldsymbol{u}_\varphi \cdot (\boldsymbol{v}\times\boldsymbol{B}) = -\boldsymbol{u}_\varphi \cdot \boldsymbol{E}_\parallel$ and introduced the function

$$\tilde{f}_D^i \equiv \int_{\varphi_0^i}^{\varphi_f^i} \tilde{I}(\varphi)\sin(\delta+\varphi)\, d\varphi \tag{17}$$

Similarly, we can find the electrodynamic torque about the center of the loop

$$\boldsymbol{M}_0^i = \int R_l \boldsymbol{u}_r \times d\boldsymbol{F}_L^i \equiv R_l^3 p_t J_0 B_0 \boldsymbol{m}_0^i \tag{18}$$

with

$$\boldsymbol{m}_0^i = -\tilde{B}_\parallel \int_{\varphi_0^i}^{\varphi_f^i} \tilde{I}\cos(\Delta+\varphi)\,\boldsymbol{u}_\varphi d\varphi = \frac{\tilde{B}_\parallel \boldsymbol{u}_x}{2}\left[m_s^i\cos\Delta + (m_c^i - \tilde{I}_{av})\sin\Delta\right] + \frac{\tilde{B}_\parallel \boldsymbol{u}_y}{2}\left[m_s^i\sin\Delta - (m_c^i + \tilde{I}_{av})\cos\Delta\right] \tag{19}$$

where $\tilde{\boldsymbol{B}}_\parallel \equiv \boldsymbol{B}_\parallel/B_0$, and we used $\boldsymbol{u}_r \times (\boldsymbol{u}_\varphi \times \boldsymbol{B}) = (\boldsymbol{u}_r \cdot \boldsymbol{B})\,\boldsymbol{u}_\varphi$ and introduced angle Δ according to $\boldsymbol{B} = \boldsymbol{B}_\parallel + \boldsymbol{B}_\perp = -B_\parallel(\cos\Delta \boldsymbol{u}_x - \sin\Delta \boldsymbol{u}_y) + B_\perp \boldsymbol{u}_z$. In Eq. (19) we also defined the function

$$m_s^i(\tilde{E}_\parallel, \delta) = \int_{\varphi_0^i}^{\varphi_f^i} \tilde{I}\sin 2\varphi d\varphi \tag{20}$$

and a similar definition for m_c^i but changing $\sin 2\varphi$ by $\cos 2\varphi$. The torque has no component in the direction normal to the loop (along $\boldsymbol{u}_z$).

The three panels of Fig. 5 show $\tilde{f}_D$, m_s and m_c versus $\tilde{E}_\parallel$ for a loop with $\delta = 0$ and an arc with $\varphi_0 = 0$ and $\varphi_f = \pi$ and several values of δ. As shown in the top panel, the normalized force $\tilde{f}_D$, which controls the decay rate during the deorbiting, is positive and increases with $\tilde{E}_\parallel$. For a loop, such a quantity does not depend on δ and it is twice the one of the arc when $\delta = 0$. The sign of m_s depends on $\tilde{E}_\parallel$ (middle panel), whereas the values of m_c for a loop with $\delta = 0$ and an arc with $\delta = \pi/2$ vanish.

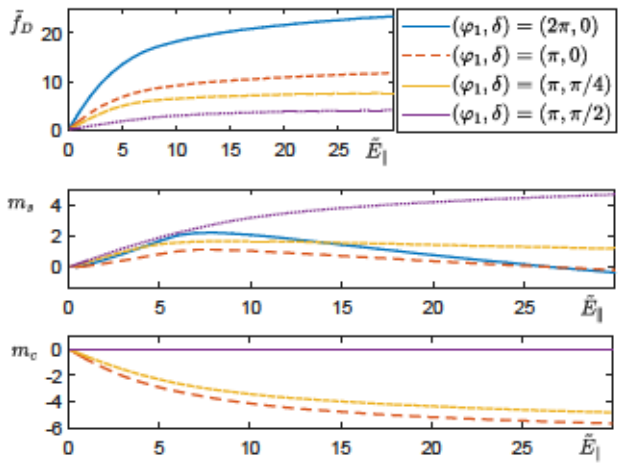

Figure 5 From the top to the bottom, the panels show $\tilde{f}_D$, m_s and m_c versus $\tilde{E}_\parallel$ for several φ_i and δ values.

For a loop without switches, i.e. the experiment in the *loop-mode*, it is more convenient to find the components of the dimensionless torque in a frame spanned by $\boldsymbol{u_1} \equiv \boldsymbol{E}_\parallel/|\boldsymbol{E}_\parallel|$ and $\boldsymbol{u_2} \equiv \boldsymbol{u}_z \times \boldsymbol{u_1}$. From Eq. (19), one finds

$$\boldsymbol{m_0} = \frac{m_s^*}{2}\left[\left(\tilde{\boldsymbol{B}}_\parallel \cdot \boldsymbol{u_2}\right)\boldsymbol{u_2} - \left(\tilde{\boldsymbol{B}}_\parallel \cdot \boldsymbol{u_1}\right)\boldsymbol{u_1}\right] \tag{21}$$

where $m_s^* \equiv m_s(\tilde{E}_\parallel, \delta = 0)$ and we used that $\tilde{I}_{av} = 0$ and $m_c(\tilde{E}_\parallel, \delta = 0) = 0$.

IV. A dynamic model of the LWT loop

Let us consider a LWT loop initially deployed in a circular and equatorial orbit of radius r_0 and let $\boldsymbol{e_x}, \boldsymbol{e_y}$ and $\boldsymbol{e_z}$ be the unit vectors of an inertial frame $\boldsymbol{S_E}$ with origin at the center of the Earth, and vectors $\boldsymbol{e_x}$ and $\boldsymbol{e_y}$ spanning the equatorial plane (see Fig. 6). For simplicity, the present analysis just considers the effect of the gravitational and electrodynamic forces and ignores other perturbations. Later refined studies should incorporate other forces, such as the aerodynamic drag, that can be important or even the dominant perturbation force depending on the particular parameter of the selected orbit.

A. Dynamics of the center of mass

After calling $\boldsymbol{r(t)}$ to the position vector of the center of the loop with respect to $\boldsymbol{S_E}$ ($|\boldsymbol{r(0)}| = r_0$), the equation of motion of the center of mass is

$$\frac{d^2\boldsymbol{r}}{dt^2} = -\frac{\mu}{r^3}\boldsymbol{r} + \frac{1}{m}\sum_{i=1}^{N_a} \boldsymbol{F}_L^i, \tag{22}$$

where N_a is the number of arcs forming the loop and μ the Earth gravitational parameter. For instance, for a loop with switches at $\varphi = 0$ and $\varphi = \pi$, one has $N_a = 2$. Hereafter we will assume that the Lorentz force is weak and it makes the orbit slowly evolve through a sequence of quasi-circular orbits with velocity $v \approx \sqrt{\mu/r}$. The evolution of the radius can then be found by taking

the dot product of Eq. (22) with the velocity $\boldsymbol{v} = \boldsymbol{dr}/\boldsymbol{dt}$

$$\frac{dr}{dt} = \frac{2r^2}{m\mu}\boldsymbol{v} \cdot \sum_{i=1}^{N_a} \boldsymbol{F}_L^i = -\frac{2r^2}{m\mu} p_t R_l^2 J_0 E_\parallel \sum \tilde{f}_D^i \tag{23}$$

Since $\tilde{f}_D > 0$, the electrodynamic force deorbits the loop. The required time to deorbit from r_0 to a final radius r_f is

$$T_D = \frac{m\mu}{2p_t R_l^2} \int_{r_f}^{r_0} \frac{dr}{r^2 J_0 E_\parallel \sum \tilde{f}_D^i} \tag{24}$$

The integral involves altitude profiles of J_0, $E_\parallel$, and $\tilde{f}_D^i$, which depends on ambient values and loop attitude. However, for the values of Table 1 and considering a characteristic value of $E_\parallel = 0.15 V/m$, Eq. (24) shows that the deorbit time is around one year. Eclipses, when the LWT is not illuminated and becomes cold, increases such a deorbit time due to lack of emitted electrons.

B. Attitude Dynamics

Since the deorbit time is much larger than the orbital period, we now analyze the attitude dynamics of the loop in equatorial orbit under the assumption of constant orbital radius, say r_0. For simplicity, the analysis is restricted to the *loop-mode* and the geomagnetic field is modeled as a nontilted and centered dipole. The loop dynamics is studied with respect to the orbital frame S_O with the origin at the center of the loop and axes spanned by the unit vectors $\boldsymbol{o_x}$, $\boldsymbol{o_y}$, and $\boldsymbol{o_z}$ along the motional electric field, the orbital velocity, and the geomagnetic field, respectively, i.e. $\boldsymbol{E} = B_0\sqrt{\mu/r_0}\boldsymbol{o_x}$, $\boldsymbol{v} = \sqrt{\mu/r_0}\boldsymbol{o_y}$, and $\boldsymbol{B} = B_0\boldsymbol{o_z}$. The angular velocity of S_O with respect to the inertial frame S_E is $\boldsymbol{\omega_{OE}} = \omega_0\boldsymbol{o_z}$, where $\omega_0 \equiv \sqrt{\mu/r_0^3}$ is the orbital angular velocity. Let us call $-\pi \leq \theta \leq \pi$, $-\pi/2 \leq \psi \leq \pi/2$, and $0 \leq \phi < 2\pi$ to the three angles that orientate frames S_L (the loop) with respect to S_O according to the following definition (see also Fig. 6)

$$\begin{pmatrix} \boldsymbol{u_x} \\ \boldsymbol{u_y} \\ \boldsymbol{u_z} \end{pmatrix} = \bar{R}_{LO} \begin{pmatrix} \boldsymbol{o_x} \\ \boldsymbol{o_y} \\ \boldsymbol{o_z} \end{pmatrix} \tag{25}$$

with $\bar{\boldsymbol{R}}_{\boldsymbol{LO}}$ the rotation matrix

$$\bar{\boldsymbol{R}}_{LO} = \begin{pmatrix} c\phi c\psi & s\phi c\theta + c\phi s\psi s\theta & s\phi s\theta - c\phi s\psi c\theta \\ -s\phi c\psi & c\phi c\theta - s\phi s\psi s\theta & c\phi s\theta + s\phi s\psi c\theta \\ s\psi & -c\psi s\theta & c\psi c\theta \end{pmatrix}, \tag{26}$$

where, for brevity, we used the notation $s\alpha = \sin\alpha$ and $c\alpha = \cos\alpha$. Therefore, the angles follow the Tait-Bryan convention; starting from the orbital frame, the loop frame is obtained after making three consecutive rotations of magnitudes θ, ψ, and ϕ around axes $\boldsymbol{o_x}$, the resulting y-axis obtained after the first rotation, and $\boldsymbol{u_z}$ (see Fig. 6).

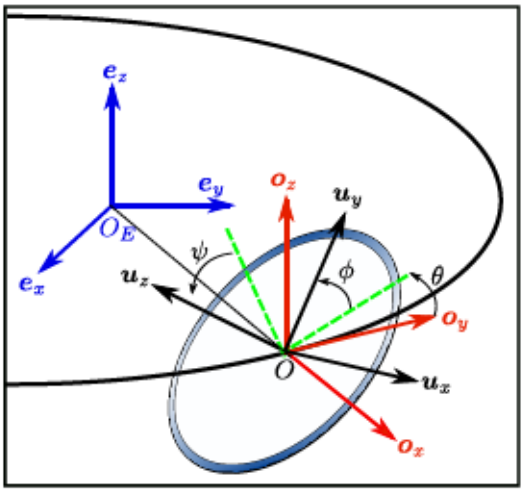

Figure 6 Frame of references and definition of the Tait-Bryan angles.

For convenience, the set of equations that governs the attitude dynamics of the loop under the effect of the gravity gradient and the Lorentz torques have been found by using Hamiltonian formulation. Appendix A shows that the normalized Hamiltonian function reads

$$\begin{aligned} \tilde{\mathcal{H}} =& \frac{(p_\psi - \sin\theta)^2}{2} + \frac{p_\phi^2}{4} + \frac{(p_\theta - p_\phi \sin\psi)^2}{2\cos^2\psi} \\ &+ \frac{\cos\theta}{\cos\psi}(p_\theta \sin\psi - p_\phi) - \frac{3\cos^2\psi}{2} + \frac{\cos^2\theta}{2} \end{aligned} \tag{27}$$

where $\boldsymbol{p_\theta}$, $\boldsymbol{p_\psi}$ and $\boldsymbol{p_\phi}$ are the generalized momenta given in Eqs. (A7)-(A9) as a function of the coordinates $\boldsymbol{\theta}$, $\boldsymbol{\psi}$, and $\boldsymbol{\phi}$ and their first derivatives. Appendix A also contains a detailed calculation

of the (normalized) generalized forces due to the electrodynamic torque. These forces are given by

$$\tilde{\mathcal{Q}}_\theta \equiv \frac{2r_0^3\mathcal{Q}_\theta}{\mu m_l R_l^2} = \epsilon m_s^* \cos\theta \sin\psi \cos\psi \tag{28}$$

$$\tilde{\mathcal{Q}}_\psi \equiv \frac{2r_0^3\mathcal{Q}_\psi}{\mu m_l R_l^2} = \epsilon m_s^* \sin\theta \tag{29}$$

$$\tilde{\mathcal{Q}}_\phi \equiv \frac{2r_0^3\mathcal{Q}_\phi}{\mu m_l R_l^2} = 0 \tag{30}$$

and they involve de dimensionless parameter $\epsilon \equiv p_l R_l J_0 B_0 r^3/\mu m_l$ and $m_s^*(\tilde{E}_\parallel)$ (computed in Sec. III D). The latter is given as a function of $\tilde{E}_\parallel$ by the solid blue line of the middle panel in Fig. 5 and depends on angle ψ because $\tilde{E}_\parallel = e_0|\cos\psi|$ with $e_0 \equiv eR_l B_0/k_B T_e \times \sqrt{\mu/r_0}$ (find details in Appendix A). For the parameters considered in Table 1, a dipole magnetic field with intensity $B_0 \approx 2.2\times10^{-5}T$, and $r_0 = 800km$, one finds $\epsilon \approx 0.041$ and $e_0 \approx 21.75$.

Using the notation $q^1 = \theta$, $q^2 = \psi$, $q^3 = \phi$, $p_1 = p_\theta$, $p_2 = p_\psi$, and $p_3 = p_\phi$, Hamilton's equations are $dq_j/d\tau = \partial\bar{\mathcal{H}}/\partial p_j$ and $dp_j/d\tau = -\partial\bar{\mathcal{H}}/\partial q_j + \tilde{\mathcal{Q}}_j$, where $\tau \equiv \omega_0 t$ is a normalized time. The angle ϕ is cyclic variable because it does not appear explicitly in $\tilde{\mathcal{H}}$ and $\mathcal{Q}_j$. The generalized force Q_ϕ also vanishes and we then have the conservation law

$$\dot{p}_\phi = 0, \tag{31}$$

where the dot denotes derivative with respect to τ. Therefore, the generalized momentum p_ϕ is constant and the dynamics of the loop are governed by

$$\dot{\theta} = \frac{p_\theta - p_\phi\sin\psi}{\cos^2\psi} + \frac{\cos\theta\sin\psi}{\cos\psi} \tag{32}$$

$$\dot{\psi} = p_\psi - \sin\theta \tag{33}$$

$$\dot{p}_\theta = p_\psi\cos\theta + \frac{\sin\theta}{\cos\psi}(p_\theta\sin\psi - p_\phi) + \frac{\epsilon}{2}m_s^*\cos\theta\sin 2\psi \tag{34}$$

$$\dot{p}_\psi = -\frac{(p_\phi^2 + p_\theta^2)\sin\psi - p_\theta p_\phi\left(1+\sin^2\psi\right)}{\cos^3\psi} - \frac{3}{2}\sin 2\psi - \frac{\cos\theta}{\cos^2\psi}(p_\theta - p_\phi\sin\psi) + \epsilon m_s^*\sin\theta \tag{35}$$

Given a value of p_ϕ, ϵ, and e_0, Eqs. (32)-(35) can be integrated numerically to find the evolution

of angles θ and ψ. It is also worth noting that the Hamiltonian does not depend explicitly on time and it evolves according to

$$\begin{aligned}\frac{d\mathcal{H}}{d\tau} = \mathcal{Q}_j \dot{q}^j =& \epsilon m_s^* \left[\cos\theta \tan\psi \left(p_\theta - p_\phi \sin\psi\right)\right. \\ &\left. + p_\psi \sin\theta + \cos^2\theta \sin^2\psi - \sin^2\theta\right] \end{aligned} \tag{36}$$

In the absence of electrodynamic torque ($\epsilon = 0$) the Hamiltonian is also conserved.

System (32)-(35) admits several equilibrium states. The most important for the experiment is $\theta = \psi = p_\theta = p_\psi = 0$ because it gives the maximum electric current and orbital decay. For such a particular state, the loop is contained in the orbital plane, $\boldsymbol{E}_\parallel = \boldsymbol{E}$, and, according to Eq. (A9), the rotation rate of the loop about $\boldsymbol{u}_z$ is $\dot{\phi} = p_\phi/2 - 1$. The stability of such equilibrium is studied by linearizing Sys. (32)-(35) and taking solutions of the type $\theta \sim \psi \sim p_\theta \sim p_\psi \sim e^{\lambda\tau}$. The result is a homogeneous system with the compatibility condition

$$\lambda^2 = \frac{-(\beta^2+4) \pm \sqrt{\beta^4 + 4\beta^2 - 12\beta + 16 + 4\epsilon^2 m_s^{*2}}}{2} \tag{37}$$

with $\beta \equiv p_\phi - 1$. For $\epsilon = 0$, Eq. (37) recovers the well-known stability result for a body with a revolution axis in circular orbit [26]. Since the term inside the square root is always positive, the equilibrium state is a saddle (unstable), i.e. there is a λ with a positive real part, if

$$\frac{-1 - \sqrt{9 + 4\epsilon^2 m_s^{*2}}}{2} < p_\phi < \frac{-1 + \sqrt{9 + 4\epsilon^2 m_s^{*2}}}{2} \tag{38}$$

Otherwise, all the eigenvalues are pure complex numbers, and the equilibrium is a center (stable). We then conclude that the dynamic state where the loop is contained in the orbital (equatorial) plane is stable if the absolute value of the angular velocity component along $\boldsymbol{u}_z$ is high enough. For instance, for zero electrodynamic torque, the equilibrium state is stable if $d\phi/dt < -2\omega_0$ or $d\phi/dt > -\omega_0$ (remember that $\dot{\phi} = p_\phi/2 - 1$). Although the electrodynamic torque increases the parametric domain of instability due to the factor $4\epsilon^2 m_s^{*2}$ in the square root, it is not difficult to spin-stabilized the equilibrium state. However, the deployment maneuver will not leave the loop at

the exact equilibrium state in a real experiment. For that reason, we now perform a brief nonlinear analysis and study separately the cases without and with electrodynamic torque.

For $\epsilon = 0$, Eqs. (32)-(35) is a Hamiltonian system with two degrees of freedom. The loop is a spinning axisymmetric object moving in a circular orbit under the action of the gravity torque, a case that has been studied in the past [6]. It is well-known that periodic, quasiperiodic, and chaotic orbits exist, and they can be visualized with a Poincaré section. For instance, we will consider the intersections of the orbits with the surface $\psi = 0$ satisfying $\dot{\psi} > 0$. Using Eq. (27), the momentum p_ψ at that surface is

$$p_\psi = \sin\theta + \sqrt{2(\mathcal{H}+1) + \sin^2\theta - p_\phi^2/2 - p_\theta^2 + 2p_\phi\cos\theta} \tag{39}$$

For given values of $\mathcal{H}$ and p_ϕ, the Poincar'e section is computed as follows. After choosing an arbitrary point in the $\theta - p_\theta$ plane, and taking $\psi = 0$ and p_ψ from Eq. (39), Eqs. (32)-(35) are integrated numerically with such initial condition. The numerical orbit is analyzed afterward to find its intersection points with the $\psi = 0$ surface and plot them in the $\theta - p_\theta$ plane.

This procedure has been implemented for several values of p_ϕ and initial conditions but fixing $\mathcal{H}_1 = \mathcal{H}_0 + 0.1$, where $\mathcal{H}_0 = p_\phi^2/4 - p_\phi - 1$ is the value of the Hamiltonian at the previously studied equilibrium state. For convenience, we also plotted with a solid blue line the frontier

$$p_\theta^{\pm}(\theta) = \pm\sqrt{2\mathcal{H} + 3 - \cos^2\theta - \frac{p_\phi^2}{2} + 2p_\phi\cos\theta}, \tag{40}$$

which is obtained by imposing that the argument of the square root in Eq. (39) should be positive. In panels (a), (b), and (d) in Fig. 7, we show the Poincare sections for $p_\phi = 2$, $p_\phi = 1.1$, and $p_\phi = -3$. For these parameter values, the equilibrium state is a center according to Eq. (38). The Poincaré sections indicate that the dynamics is regular. For values of p_ϕ where the equilibrium is a saddle, the phase space is a mix of regular and chaotic dynamics [see panel (c) with $p_\phi = 0.9$]. A detailed analysis revealed the typical appearance of regular islands and chains of islands surrounded by a sea of chaos.

According to Fig. (7), regular and bounded orbits happen in the neighborhood of the equilibrium

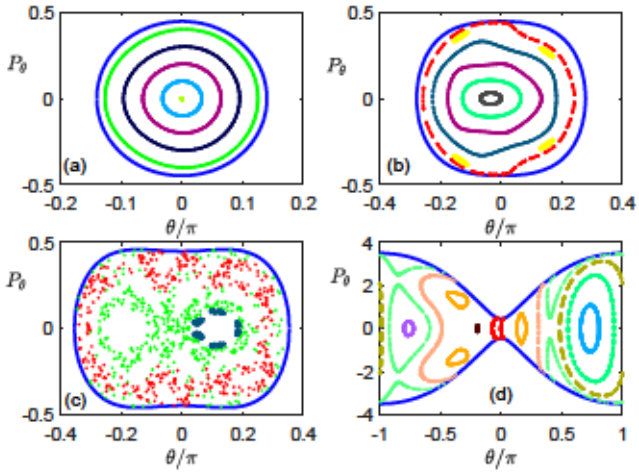

Figure 7 Poincare sections with $\epsilon = 0$ and $\mathcal{H} = \mathcal{H}_1$. Panels (a) to (d) correspond to $p_\phi = 2, 1.1, 0.9$, and -3, respectively.

state if the spin velocity belongs to the stable domain and there is no electrodynamic torque. Switching on the electric current in the loop does not seem to modify this conclusion, as shown in the Poincaré sections presented in panels (a), (b) and (d) in Fig. 8. They correspond to Poincaré sections of the orbits with the $\psi = 0$ surface for $\epsilon = 0.041$ and $p_\phi = 2, 1.1, -3$, respectively. Again, panel (c) is the Poincare section with $p_\phi = 0.9$ (regime with unstable equilibrium state). Similar to Fig. 7, all the initial conditions of the trajectories have $\psi = 0$ and Hamiltonian $\mathcal{H}_1$ and, for convenience, the frontier given by Eq. (40) has also been plotted with a solid blue line. However, since $\epsilon \neq 0$ and the Hamiltonian function is not conserved [see Eq. (36)], there are orbit's intersections outside the region delimited by such a frontier.

A comparison of Figs. 7 and 8 reveal some interesting effects due to the Lorentz torque in phase space regions away from the origin. The most evident is for the case $p_\phi = -3$ [panels (d)]; all the orbits are regular in the absence of Lorentz torque (Fig. 7), but chaotic motions appear outside the origin for finite electric current (Fig. 8). The orbits also explore a broader region of the phase space for $\epsilon \neq 0$. Panels (b) in Figs. 7 and 8 also show that the Lorentz force increases the complexity of the phase space.

V. Conclusions

This work considered an in-orbit experiment with an electrodynamic tether loop coated with a low work function material. Thanks to the tether-to-plasma relative motion and the geomagnetic

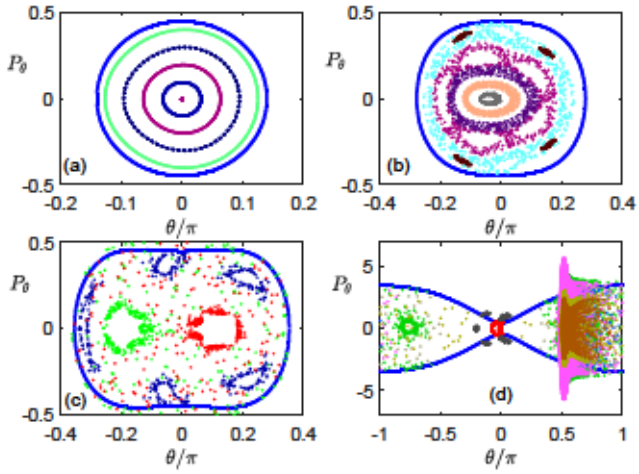

Figure 8 Poincare sections with $\epsilon = 0.041$ and $\mathcal{H} = \mathcal{H}_1$. Panels (a) to (d) correspond to $p_\phi = 2, 1.1, 0.9$, and -3, respectively.

field, the tether is polarized with respect to the plasma, yielding to anodic and cathodic tether segments that capture and emit electrons, respectively. The latter happens thanks to a coating dedicated to emit electrons through thermionic and photoelectric effects if the tether is illuminated by the Sun. The Lorentz drag, exerted by the ambient magnetic field on the tether current, appears without using power and consumable. Two different modes of operation have been proposed and discussed: (i) letting the electric current flow freely in the loop, which yields zero average current but non-vanishing Lorentz force, and (ii) interrupting the current at certain tether points, thus forming several electric arcs. In addition to the electrodynamic model, the study presents the equations governing the attitude dynamic of the loop under the presence of the Lorentz and the gravity gradient torques. A Hamiltonian formulation approach was used because it makes transparent key features like the presence of conserved quantities.

The theoretical models have been particularized for an aluminum tether coated with a material of work function 1.4eV, operating at 500K, and initially flying in an equatorial orbit of altitude 800km. Due to mechanical and electrodynamic considerations, a torus-like tether with an annular cross-section seems to be advantageous. Proposed values of the torus radius, tether external radius and thickness are $20m$, $1.5cm$ and $30\mu m$. The mass of such a tether is around 1 kg, thus indicating that a very light experiment could be achieved. It is found from Fig. 3 and panel (a) in Fig. 5, that the maximum electric current and drag force can be in the order of $10^{-2}A$ and $10^{-5}N$ and

the deorbit time would be below a year. On the other hand, the Lorentz torque does not break the conservation of the component of the angular momentum along the axis of symmetry of the loop (p_ϕ). As a consequence, the equations governing the attitude of the loop is a dynamical system with just two degrees of freedom. Special attention was paid to the dynamic state with the loop contained in the orbital (equatorial) plane and spinning around its symmetry axis because it yields the highest electric current and orbital decay. Although the electrodynamic torque enlarges the spinning velocity range where such an equilibrium state is unstable, the analysis indicates that it would be relatively easy to have a spin-stabilized loop. For instance, for typical values of the electrodynamic torque, it would be enough to make the loop spins with a finite angular velocity in the same direction as the orbital angular velocity. The Poincaré sections with and without electrodynamic torque reveal some interesting features in the non-linear regime: the phase space region where the loop will remain close to the equilibrium state is broad if p_ϕ belongs to the range where the equilibrium is a stable.

The analysis shows that, thanks to the loop shape, the in-orbit experiment can provide abundant and valuable scientific information about the electrodynamic and dynamic behaviors of low work function tethers. First, current, temperature and voltage profiles could be measured in real time during the full deorbiting if ammeters and thermocouples are intercalated at several tether points, and voltmeters are connected between few tether points and a control unit. Second, a Langmuir probe, 3-axis magnetometers, and GNSS on-board the control unit can provide plasma density, magnetic field, motional electric field and tether position, velocity, and attitude. The control unit should also include telemetry and telecommand in order to send the scientific data to the ground segment and control the two modes of operation of the tether (loop or arcs). Some scientific questions on tether-plasma interactions, low work function materials, and tether dynamics that could be addressed by confronting the experimental data with the theoretical models presented in this paper are: (i) How accurate is our actual theoretical model for electron collection and emission (function $J(V)$ obtained from Vlasov-Poisson simulations), (ii) How accurate are the equations governing the current and voltage profiles along a bare electrodynamic tether ?, (iii) How fast is the degradation of the coating in space conditions, including both work function and optical properties ?, (iv) What is the efficiency of a low work function tether in de-orbiting scenarios ?, (v) What is the long term effect

of the Lorentz torque on the attitude of an extended body like a tether ?. Although this study was restricted to the current and voltage profiles in stationary conditions, the transient behavior from the loop mode to the arc mode and vice-versa could also be modeled and confronted to experimental data. Finally, in case another spacecraft would fly following the experiment, the properties of the waves excited in the plasma by the loop could be also investigated.

Our analysis relies on a set of rational assumptions that allowed to keep the problem treatable from a semi-analytical point of view and uncover interesting features of the experiment. However, there are several effects that may be included in more refined analysis. For instance, the aerodynamic drag may be important for low altitudes. Additionally, in order to compute the deorbit time accurately, it would be necessary to couple the dynamic equations of the center of mass with the attitude equations and complement them with models for the ambient parameters, such as plasma properties and magnetic field. A database with a collection of $\boldsymbol{j-eV/kT_e}$ curves would also be needed to compute the current and voltage profiles correctly at every time step during the integration.

Acknowledgments

This work was initially supported by Agencia Estatal de Investigación (Ministerio de Ciencia, Innovación y Universidades of Spain) under the project ESP2017-82092-ERC (AEI) and continued thanks to funding received from the European Union´s Horizon 2020 research and innovation programme under grant agreement No 828902 (E.T.PACK project). GSA work is supported by the Ministerio de Ciencia, Innovación y Universidades of Spain under the Grant RYC-2014-15357. SN work is supported by Comunidad de Madrid (Spain) under the Grant 2018/T2IND/11352. The authors thank X. Chen for providing the curve in Fig. 2 and J. R. Sanmartin for his valuable comments.

Appendix A: EQUATIONS OF MOTIONS

The angular velocity of the loop with respect to the orbital frame S_0 reads

$$\begin{aligned}\boldsymbol{\omega}_{LO} =&\sqrt{\frac{\mu}{r^3}}\left[\left(\dot{\psi}s\phi+\dot{\theta}c\psi c\phi\right)\boldsymbol{u}_x+\left(\dot{\psi}c\phi-\dot{\theta}c\psi s\phi\right)\boldsymbol{u}_y+\right.\\&\left.\left(\dot{\phi}+\dot{\theta}\sin\psi\right)\boldsymbol{u}_z\right]\end{aligned}\tag{A1}$$

where the dot denotes the derivative with respect to the normalized time $\tau \equiv \omega_0 t$ with $\omega_0 \equiv \sqrt{\mu/r_0^3}$. The Lagrangian of the loop relative to the orbital frame, $\mathcal{L} = \mathcal{T} - \mathcal{U}$, includes the kinetic energy

$$\begin{aligned}\mathcal{T} &= \frac{1}{2}\boldsymbol{\omega}_{LO}\cdot\bar{\boldsymbol{I}}_O\cdot\boldsymbol{\omega}_{LO}\\&= \frac{\mu m_l R_l^2}{4r^3}\left[\dot{\psi}^2+\dot{\theta}^2\cos^2\psi+2\left(\dot{\phi}+\dot{\theta}\sin\psi\right)^2\right]\end{aligned}\tag{A2}$$

and the potential energy, $\mathcal{U} = \mathcal{U}_G + \mathcal{U}_I$. The gravitational potential $\mathcal{U}_G$ up to terms of order $(R_l/r_0)^3$ is (see for instance [16])

$$\mathcal{U}_G \approx -\frac{\mu}{r_0}\int\left[1-\frac{\boldsymbol{r}'\cdot\boldsymbol{o}_x}{r_0}+\frac{3}{2}\left(\frac{\boldsymbol{r}'\cdot\boldsymbol{o}_x}{r_0}\right)^2-\frac{|\boldsymbol{r}'|^2}{2r_0^2}\right]dm\tag{A3}$$

and the potential of the apparent forces due to the non-Galilean nature of S_O is

$$\mathcal{U}_I = \int\left\{\boldsymbol{a}_O\cdot\boldsymbol{r}'-\frac{1}{2}\left(\boldsymbol{\omega}_{OE}\times\boldsymbol{r}'\right)^2-\boldsymbol{\omega}_{OE}\cdot\left(\boldsymbol{r}'\times\boldsymbol{v}'\right)\right\}dm\tag{A4}$$

Here $\boldsymbol{a}_0 \approx -\mu/r_0^2\boldsymbol{o}_x$ is the acceleration of the center of the loop, $\boldsymbol{\omega}_{OE} = \sqrt{\mu/r_0^3}\boldsymbol{o}_z$ is the angular velocity of the orbital frame with respect to the inertial frame, and $\boldsymbol{r}' = R_l\boldsymbol{u}_r$ and $\boldsymbol{v}' = R_l\boldsymbol{\omega}_{LO}\times\boldsymbol{u}_r$ are the position and velocity vectors with respect to S_0 of a mass element dm of the loop. After

some cumbersome calculations, one finds

$$\begin{aligned}\mathcal{U}_G =& -\frac{\mu m_l}{r_0}\left[1+\frac{1}{2}\frac{R_l^2}{r_0^2}\left(\frac{3}{2}\cos^2\psi-1\right)\right]\\ \mathcal{U}_I =& -\frac{\mu m_l R_l^2}{4r_0^3}\left[1+\cos^2\theta\cos^2\psi+2\dot{\psi}\sin\theta\right.\\ &\left.+\dot{\theta}\cos\theta\sin 2\psi+4\dot{\phi}\cos\theta\cos\psi\right]\end{aligned} \tag{A5}$$

Therefore, after excluding constant terms, the normalized Lagrangian function is

$$\begin{aligned}\tilde{\mathcal{L}} \equiv \frac{2r_0^3\mathcal{L}}{\mu m_l R_l^2} =& \frac{1}{2}\left[\dot{\psi}^2+\dot{\theta}^2\cos^2\psi+2\left(\dot{\phi}+\dot{\theta}\sin\psi\right)^2\right.\\ &+2\dot{\psi}\sin\theta+\cos^2\psi\left(3+\cos^2\theta\right)\\ &\left.+\dot{\theta}\cos\theta\sin 2\psi+4\dot{\phi}\cos\theta\cos\psi\right]\end{aligned} \tag{A6}$$

and the generalized momenta

$$p_\theta \equiv \frac{\partial\tilde{\mathcal{L}}}{\partial\dot{\theta}} = \dot{\theta}\left(1+\sin^2\psi\right)+2\dot{\phi}\sin\psi+\cos\theta\sin\psi\cos\psi \tag{A7}$$

$$p_\psi \equiv \frac{\partial\tilde{\mathcal{L}}}{\partial\dot{\psi}} = \dot{\psi}+\sin\theta \tag{A8}$$

$$p_\phi \equiv \frac{\partial\tilde{\mathcal{L}}}{\partial\dot{\phi}} = 2\left[\dot{\phi}+\dot{\theta}\sin\psi+\cos\theta\cos\psi\right] \tag{A9}$$

For convenience, hereafter we will use the notation $q^1=\theta$, $q^2=\psi$, $q^3=\phi$, $p_1=p_\theta$, $p_2=p_\psi$, and $p_3=p_\phi$ and Einstein summation convention. The normalized Hamiltonian function takes the form

$$\tilde{\mathcal{H}} \equiv \dot{q}^j p_j - \tilde{\mathcal{L}} \tag{A10}$$

and its explicit form in terms of the coordinates and the momenta is given in Eq. (27)

On the other hand, the Lorentz torque appears in the equations of motion through the generalized force components

$$\mathcal{Q}_j = \boldsymbol{M_0}\cdot\frac{\partial\boldsymbol{\omega}_{LO}}{\partial\left(dq^j/dt\right)} \tag{A11}$$

In order to find them, we first compute the components of $\boldsymbol{E}_\parallel$ and $\boldsymbol{B}_\parallel$ in body axis

$$\frac{\boldsymbol{E}_\parallel}{B_0}\sqrt{\frac{r_0}{\mu}} = \boldsymbol{o_x} - (\boldsymbol{o_x}\cdot\boldsymbol{u_z})\,\boldsymbol{u_z} = \cos\psi\,(\cos\phi\boldsymbol{u_x} - \sin\phi\boldsymbol{u_y}) \tag{A12}$$

$$\begin{aligned}\frac{\boldsymbol{B}_\parallel}{B_0} =& \boldsymbol{o_z} - (\boldsymbol{o_z}\cdot\boldsymbol{u_z})\,\boldsymbol{u_z} = \\ & (\sin\theta\sin\phi - \cos\theta\sin\psi\cos\phi)\,\boldsymbol{u_x} + \\ & (\sin\theta\cos\phi + \cos\theta\sin\psi\sin\phi)\,\boldsymbol{u_y}\end{aligned} \tag{A13}$$

Therefore, we have $\boldsymbol{E}_\parallel = B_0\sqrt{\mu/r_0}|\cos\psi|$, and $\boldsymbol{u_1} = \boldsymbol{E}_\parallel/|\boldsymbol{E}_\parallel| = \cos\phi\boldsymbol{u_x} - \sin\phi\boldsymbol{u_y}$ and $\boldsymbol{u_2} = \boldsymbol{u_z}\times\boldsymbol{u_1} = \sin\phi\boldsymbol{u_x} + \cos\phi\boldsymbol{u_y}$. Using these results in Eq. (21) yields

$$\boldsymbol{m_0} = \frac{m_s^*}{2}\,(\cos\theta\sin\psi\boldsymbol{u_1} + \sin\theta\boldsymbol{u_2}) \tag{A14}$$

The substitution of Eq. (A14) in Eq. (18), and then using Eq. (A11) yield the generalized forces in (28)-(30).

REFERENCES

[1] VS Aslanov and AS Ledkov. Dynamics of Tethered Satellite Systems. In *Dynamics of Tethered Satellite Systems*, Woodhead Publishing in Mechanical Engineering, pages 1–331. 2012. ISBN 978-0-85709-600-5. doi: {10.1533/9780857096005}.

[2] V.V. Beletsky and E.M. Levin. Stability of a ring of connected satellites. *Acta Astronautica*, 12 (10):765 – 769, 1985. ISSN 0094-5765. doi: https://doi.org/10.1016/0094-5765(85)90093-1. URL `http://www.sciencedirect.com/science/article/pii/0094576585900931`.

[3] L. Bergamin, D. Izzo, and A. Pinchook. Propellantless propulsion by partially shielded current. *57th International Astronautical Congress*, IAC-06-C4.6.05, 2006.

[4] Xin Chen and G. Sanchez-Arriaga. Orbital motion theory and operational regimes for cylindrical emissive probes. *Physics of Plasmas*, 24(2):023504, 2017. doi: 10.1063/1.4975088. URL `https://doi.org/10.1063/1.4975088`.

[5] E. Choiniere. Theory and experimental evaluation of a consistent steady-state kinetic model for 2-d conductive structures in ionospheric plasmas with application to bare electrodynamic tethers in space, 2004.

[6] Ardéshir Guran, Xiaohua Tong, and F.P.J. Rimrott. Instabilities in a spinning axi-symmetric rigid satellite. *Mechanics Research Communications*, 18(5):287 – 291, 1991. ISSN 0093-6413. doi: https://doi.org/10.1016/0093-6413(91)90010-T. URL http://www.sciencedirect.com/science/article/pii/009364139190010T.

[7] M. Holderman and E Henderson. *Nautilus-X Multi-Mission Space Exploration Vehicle*. NASA Johnson Space Center, 2011. URL http://www.scribd.com/doc/51592987/Nautilus-X-Holderman-1-26-11.

[8] Panfeng Huang, Binbin Liu, and Fan Zhang. Configuration maintaining control of three-body ring tethered system based on thrust compensation. *Acta Astronautica*, 123:37 – 50, 2016. ISSN 0094-5765. doi: https://doi.org/10.1016/j.actaastro.2016.03.005. URL http://www.sciencedirect.com/science/article/pii/S0094576516302077. Special Section: Selected Papers from the International Workshop on Satellite Constellations and Formation Flying 2015.

[9] Pekka Janhunen. Electric sail for spacecraft propulsion. *Journal of Propulsion and Power*, 20(4): 763–764, Jul 2004. ISSN 0748-4658. doi: 10.2514/1.8580. URL https://doi.org/10.2514/1.8580.

[10] R.D. Johnson, C.H. Holbrow, United States. National Aeronautics, Space Administration, and American Society for Engineering Education. *Space Settlements: A Design Study*. Number n.º 413 in NASA SP. Scientific and Technical Information Office, National Aeronautics and Space Administration, 1977. URL https://books.google.es/books?id=ZOsCAAAAIAAJ.

[11] M Keshmiri, AK Misra, and VJ Modi. General formulation for N-body tethered satellite system dynamics. *Journal of Guidance Control and Dyanmics*, 19(1):75–83, JAN-FEB 1996. ISSN 0731-5090. doi: {10.2514/3.21582}.

[12] J. G. Laframboise. *Theory of Spherical and Cylindrical Langmuir Probes in a Collisionless, Maxwellian Plasma at Rest*. PhD thesis, University of Toronto (Canada)., 1966.

[13] E. M. Levin. Electrodynamic structure. patent us 2007/0210213 a1, 2007.

[14] Gangqiang Li, Zheng H. Zhu, Stephane Ruel, and S.A. Meguid. Multiphysics elastodynamic finite element analysis of space debris deorbit stability and efficiency by electrodynamic tethers. *Acta Astronautica*, 137:320 – 333, 2017. ISSN 0094-5765. doi: https://doi.org/10.1016/j.actaastro.2017.04.025. URL http://www.sciencedirect.com/science/article/pii/S0094576517300449.

[15] E. C. Lorenzini. Novel Tether-Connected Two-Dimensional Structures for Low Earth Orbits. *Journal of the Astronautical Sciences*, 36(4):389–405, 1988.

[16] J. Pelaez, E. C. Lorenzini, O. Lopez-Rebollal, and M. Ruiz. A new kind of dynamic instability in electrodynamic tethers. *The Journal of the Astronautical Sciences*, 48:449–476, 2000.

[17] O.W. Richardson. *The emission of electricity from hot bodies*. Longmans, Green, and co.., 1916.

[18] A. Rocchi and M. Lavagna. Versatile Electro-Dynamic Tethers Dynamics Simulator for Debris Mitigation Tool Design. *13th Symposium on Advanced Technologies in Robotic and Automation*, Paper 209B-96077:Noordwijk, The Netherlands, 2015.

[19] G. Sánchez-Arriaga and X. Chen. Modeling and Performance of Electrodynamic Low-Work-Function Tethers with Photoemission Effects. *Journal of Propulsion and Power*, 34(1):213–220, 2018. doi: https://doi.org/10.2514/1.B36561.

[20] G. Sanchez-Arriaga and J. R. Sanmartin. Magnetic pumping of whistler waves by tether current modulation. *Journal of Geophysical Research: Space Physics*, 115(A2):n/a–n/a, 2010. ISSN 2156-2202. doi: 10.1029/2009JA014478. URL http://dx.doi.org/10.1029/2009JA014478. A02311.

[21] G. Sánchez-Arriaga, X. Chen, and E.C Lorenzini. Optimal Design and Deorbiting Performance of Thermionic Bare Tethers in Geostationary Transfer Orbits. *Journal of Propulsion and Power*, 33(2): 425–432, 2017. doi: 10.2514/1.B36202.

[22] J. R. Sanmartín and R. D. Estes. The Orbital-Motion-Limited Regime of Cylindrical Langmuir Probes. *Physics of Plasmas*, 6:395–405, January 1999. doi: 10.1063/1.873293.

[23] J. R. Sanmartín and R. D. Estes. Interference of parallel cylindrical langmuir probes. *Physics of Plasmas*, 8(9):4234–4239, 2001. doi: 10.1063/1.1390332.

[24] J. R. Sanmartin, M. Martinez-Sanchez, and E. Ahedo. Bare Wire Anodes for Electrodynamic Tethers. *Journal of Propulsion Power*, 9:353–360, 1993.

[25] Juan R. Sanmartin and Enrico C. Lorenzini. Role of superconducting shields in electrodynamic propulsion. *Journal of Propulsion and Power*, 24(4):851–854, Jul 2008. ISSN 0748-4658. doi: 10.2514/1.30433. URL https://doi.org/10.2514/1.30433.

[26] W.T. Thomson. Spin stabilization of attitude against gravity torque. *Journal of Astronautical Science*, 9:31–33, 01 1962.

[27] J. D. Williams, J. R. Sanmartín, and L. P. Rand. Low Work-Function Coating for an Entirely Propellantless Bare Electrodynamic Tether. *IEEE Transactions on Plasma Science*, 40:1441–1445, May 2012. doi: 10.1109/TPS.2012.2189589.

[28] Jun Zhao, Zhiqin Cai, and Zhaohui Qi. Dynamics of Variable-Length Tethered Formations near Libration Points. *Journal of Guidance, Control, and Dynamics*, 33(4):1172–1183, JUL-AUG 2010. ISSN 0731-5090. doi: {10.2514/1.47138}.